

A Selective Hybrid Stochastic Strategy for Fuel-Cell Multi-Parameter Identification

Massimo Guarnieri ^{a,*}, Enrico Negro ^a, Vito Di Noto ^a, Piergiorgio Alotto ^a

^aDepartment of Industrial Engineering – University of Padua - Padua, Italy

Corresponding author: Massimo Guarnieri, massimo.guarnieri@unipd.it

ABSTRACT

The *in situ* identification of fuel-cell material parameters is crucial both for guiding the research for advanced functionalized materials and for fitting multiphysics models, which can be used in fuel cell performance evaluation and optimization. However, this identification still remains challenging when dealing with direct measurements. This paper presents a method for achieving this aim by stochastic optimization. Such techniques have been applied to the analysis of fuel cells for ten years, but typically to specific problems and by means of semi-empirical models, with an increased number of articles published in the last years. We present an original formulation that makes use of an accurate zero-dimensional multi-physical model of a polymer electrolyte membrane fuel cell and of two cooperating stochastic algorithms, particle swarm optimization and differential evolution, to extract multiple material parameters (exchange current density, mass transfer coefficient, diffusivity, conductivity, activation barriers ...) from the experimental data of polarization curves (i.e. *in situ* measurements) under some controlled temperature, gas back pressure and humidification. The method is suitable for application in other fields where fitting of multiphysics nonlinear models is involved.

Keywords

Fuel cell, *In situ* characterization, Material characterization, Multiphysics modeling, Multiple identification, Stochastic methods

1. Introduction

1.1. Fuel Cell perspectives

As electricity sources which do not undergo the Carnot cycle limitations, Fuel Cells (FCs) are appealing for a number of applications within the future energy framework. Solid Oxide FCs (SOFCs) and Molten Carbonate FCs (MCFCs), working at high temperatures (around 600°C), promise to be competitive in the stationary middle-to-micro combined heat and power production (CHP). Proton Exchange Membrane fuel cells (PEMFCs) constitute the more promising technology for mobility, with early applications in niche sectors (e.g. forklifts, golf carts, submarines). As regards road mobility, PEMFC-powered urban bus fleets, capable of longer ranges than batteries, have been tested and introduced in big cities (e.g. London, Hamburg, Barcelona, Stockholm, Oslo, Porto, Stuttgart, Amsterdam, Luxemburg, Madrid, Aberdeen, Reykjavík, and Perth). In these years, the electric car market is expanding, but battery-powered models still lack competitiveness as regards range, recharge time, lifetime, and cost. PEMFC-powered cars, capable of longer ranges and faster refueling, are now entering mass production. The Hyundai ix35 (FC version of the Tucson SUV), commercialized since 2013, is the first of them and has been followed in 2014–5 by the Toyota Mirai FCV, whose two 122-liter 70-MPa hydrogen tanks provide a 650 km range. Honda and Mercedes-Benz are going to sell their models FCX Clarity II (35-MPa tanks for 390-km range) and F-Cell (70-MPa tanks for 678-km range) within 2016 and 2017, respectively. As regards devices working at lower power levels, the sensational spread of portable electronics has been backed by batteries with high energy density, but small-sized Direct Methanol Fuel Cells (DMFCs) are emerging as a competitive alternative for assuring extended durations. Success in all these sectors relies on the availability of more efficient, more durable and cheaper next-generation FCs based on new materials and architectures.

1.2. FC material characterization

Since fuel cells present a stratified structure of thin layers made of different materials, analyzing their behavior requires the full characterization of these materials, i.e. the determination of their chemical, physical, thermal, and electrical parameters [1]. Unfortunately, they are hard to measure in real operating conditions. These physical parameters are also needed in FC models, which allow the fast exploration of different operating scenarios and can be used in the research of optimized structural design and operating conditions [2,3]. The systems of equations involved (Nernst equation, Butler-Volmer equation, Darcy's equation, Fourier's law, Ohm's law, ...) are strongly non-linear, causing the models to be extremely sensitive to parameter variations and uncertainties. Careful *ex situ* measurements can be performed by means of a number of diagnostic techniques, e.g. cyclic voltammetry with the thin-film rotating ring-disc electrode (CV-TF-RRDE) setup, electrochemical impedance spectroscopy (EIS), and broadband electrical spectroscopy (BES) [4–8]. However, the transferability of their results to operative fuel cells raises a number of issues. Conversely, *in situ* measurements can provide meaningful operational values, but very few, often complicated and cumbersome, techniques are available to determine a limited number of parameters, e.g. EIS, neutron radiography, and voltammetric and chronoamperometric approaches in the “driven-cell” mode [4,5,9].

1.3. Numerical optimization search approach

A different approach consists in multiple parameter identification from a rich sample of experimental data obtained at different values of temperature, and gas pressure and humidity. Unfortunately, this approach is not so easy to implement, because the problem becomes increasingly difficult as the number of parameters increases, resulting in the *curse of dimensionality* issue [10]. This challenge can be faced with mathematical optimization, which typically consists in a minimization or maximization problem [11]. In the former case, given a function f (called fitness, objective, quality, or cost function) that maps a domain A (search space) of an n -dimensional Euclidean space into real numbers, optimization aims at finding the element x_0 of A such that $f(x_0)$ is smaller than every other $f(x)$ for x in A :

$$\begin{aligned} \text{given } f(x): & \quad A \rightarrow \mathbf{R} \quad A \subseteq \mathbf{R}^n \\ \text{seek } x_0 \in A: & \quad f(x_0) \leq f(x) \quad \forall x \neq x_0 \end{aligned} \quad (1)$$

The optimization problem can be similarly formulated as a mathematical maximization. When using mathematical optimization for model parameter identification, x is the n -dimensional vector whose elements are the unknown parameters and $f(x)$ consists of a proper error among the computed performance values provided by a parameter-based model and measured performance data. Optimization problems are typically constrained, in the sense that A is given with a number of constraints and is also typically burdened by model non-linearity, as is the case of an FC model, which results in the non-convexity of f and consequent local minima x^* [12]:

$$f(x^*) \leq f(x) \quad \|x - x^*\| \leq \delta \quad (2)$$

Moreover, large problems lead to high computational cost. Given the problems of curse of dimensionality, presence of local minima and computational costs, smart strategies can find good solutions, if not the absolute best one, which actually may be impossible to find. Although the *no-free-lunch* theorem shows that “any two optimization algorithms are equivalent when their performance is averaged across all possible problems” [13], efficient optimizers exist which allow to solve our specific problem of finding only a domain-specific solution.

Stochastic methods have been introduced in the analyses of FCs in the last decade and their use has been strongly increasing in the last three years. The researches published so far aim at exploring the capability of stochastic methods in achieving good fittings of PEMFC polarization curves and resort to simplified empirical PEMFC models, used as black boxes. Those stochastic methods demonstrate to be efficient at that aim, since their results depend on some optimization parameters which must be trimmed at the

experimental polarization curves. In these conditions, fitting a set of empirical parameters to match a given polarization curve is not a hard task for numerical optimizers, but the usefulness of the results is limited. By using a proper number of unknown parameters (5–7), they provide enough flexibility for fitting purposes without introducing *duplicity problems* (i.e. multiple fitting solutions which can appear when many unknowns are sought). However, duplicity is not crucial, because empirical parameters have no direct physical meaning. Conversely, the algorithm that we present, built over an early investigation on the capability of stochastic methods to deal with FCs [14], aims at identifying several physical parameters of the materials of a PEMFC by means of an optimization approach. At this aim, we use a detailed multi-physical performance model that employs such parameters and takes into account some physical control quantities [15].

In the following sections, we first present the PEMFC performance model, consisting of non-linear equations, which provides the computed performance (the PEMFC polarization curves) at different values of physical control quantities (temperature, gas pressure and humidity) making use of the unknown parameters. Then, we present the *selective hybrid stochastic algorithm* that we have developed for identifying the unknown parameters. It consists of a *hybrid stochastic method* complemented with a *selective strategy* for coping with the duplicity problem. Finally, an example of multi-parameter identification is presented.

2. PEMFC multiphysics performance model

The model for the stochastic identification must strike a balance between opposite requirements. On one hand it should be extremely rich in order to be able to represent the complete behavior of the cell, i.e. a multiphysical, three-dimensional model, described by partial differential equations (PDEs) and characterized by a large number of physical parameters which can capture the detailed distribution of the physical quantities inside the cell and their time evolution. On the other hand it should be sufficiently simple to be suitable for being included in a stochastic optimization loop, i.e. the model should be numerically computable in a very short time, considering the CPU power at hand, and it should be characterized by a relatively small number of parameters in order to avoid the *curse of dimensionality* issue. Here we resort to a zero-dimensional stationary model that avoids PDEs and their inherent computational burden in order to match these conflicting requirements and to run the algorithm on a standard PC.

2.1. Open circuit emf E_{OC}

The hydrogen oxidation reaction (HOR) occurring at the anode catalyst layer (CL) and the oxygen reduction reaction (ORR) at the cathode catalyst layer



are segregated by the membrane (i.e. the proton exchange membrane, PEM, Fig. 1), allowing the development of the cell's reversible voltage E (i.e. the cell's electromotive force, emf). According to the Nernst equation, E varies with temperature T and gas pressures $p_{\text{H}_2}, p_{\text{O}_2}$ (or equivalently, with concentrations $c_{\text{H}_2}, c_{\text{O}_2}$) [16]:

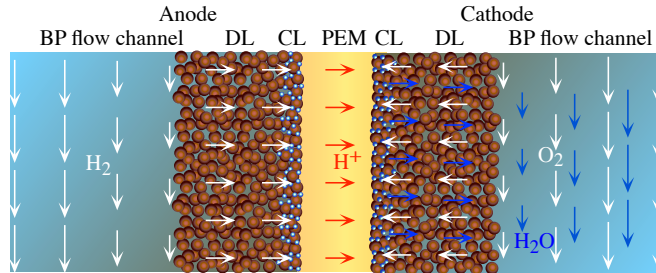


Fig. 1. Scheme of PEMFC with anode and cathode flow channels of bipolar plates (BPs), diffusion layer (DLs), catalyst layers (CLs), and proton exchange membrane (PEM). Convective (in BPs) and diffusive (in DLs) fluid flows are sketched.

$$E = E^0 + \Delta E_s(T) + \Delta E_c(T, p_{H_2}, p_{O_2}) \quad (4)$$

where $E^0 = 1.229$ V is the value at standard temperature $T^0 = 298.15$ K and pressure $p^0 = 100$ kPa, ΔE_s is the entropic variation, and ΔE_c is the variation related with gas pressures and hence with gas concentrations. In order to allow an accurate modeling over a wide temperature range, ΔE_s is calculated as

$$\Delta E_s = \frac{1}{nF} \int_{T^0}^T \Delta \hat{s}(T) dT = \frac{\Delta T}{nF} \sum_i \Delta \hat{s}(T_i) \quad (5)$$

rather than with the often used linearized expression $(\Delta \hat{s}/nF)(T - T^0)$. In (5), $F = 96485$ C/mol is the Faraday constant, $n = 2$ is the number of charge carriers per reaction, according to (3), and $\Delta \hat{s}(T_i)$ are molar reaction entropy values which are tabulated in the literature [17]. By introducing the ‘‘bulk’’ (undisturbed) concentrations \bar{c}_{H_2} and \bar{c}_{O_2} , ΔE_c can be split into two terms:

$$\begin{aligned} \Delta E_c &= \frac{RT}{nF} \ln \left[\left(\frac{c_{H_2}}{c_{H_2}^0} \right) \left(\frac{c_{O_2}}{c_{O_2}^0} \right)^{0.5} \right] = \\ &= \frac{T}{f_e} \ln \left[\left(\frac{\bar{c}_{H_2}}{c_{H_2}^0} \right) \left(\frac{\bar{c}_{O_2}}{c_{O_2}^0} \right)^{0.5} \right] + \frac{T}{f_e} \ln \left[\left(\frac{c_{H_2}}{\bar{c}_{H_2}} \right) \left(\frac{c_{O_2}}{\bar{c}_{O_2}} \right)^{0.5} \right] = \\ &= \Delta E_{co} + \Delta E_{cl} \end{aligned} \quad (6)$$

Here $R = 8.314$ J/mol·K is the gas constant and $f_e = nF/R = 23,210$ K/V. ΔE_{co} , which depends on \bar{c}_x/c_x^0 , occurs whenever the bulk concentrations differ from standard-condition values, also in a no-load state. ΔE_{cl} , which depends on c_x/\bar{c}_x , occurs as the concentrations at the electrochemical reaction sites (i.e. the triple phase boundaries, TPBs) inside the catalyst layers (CLs) differ from their bulk concentrations, due to gradients which appear in the presence of molar flow, namely, in load conditions. According to (4), (5), and (6), the cell’s open circuit emf is:

$$E_{OC} = E^0 + \frac{1}{nF} \int_{T^0}^T \Delta \hat{s}(T) dT + \frac{T}{f_e} \ln \left[\left(\frac{\bar{c}_{H_2}}{c_{H_2}^0} \right) \left(\frac{\bar{c}_{O_2}}{c_{O_2}^0} \right)^{0.5} \right] \quad (7)$$

E_{OC} differs from the open circuit voltage (OCV) because of gas crossover through the membrane that also occurs in no-load condition (Subsection 2.6). Moreover, in steady-state load conditions, the cell voltage V differs from E_{OC} and varies with the electric current density j due to ΔE_{cl} and other voltage drops ΔV_k (namely, overpotentials η) [18]:

$$V(j) = E_{OC} - \Delta V_{aa} - \Delta V_{ac} - \Delta V_{ca} - \Delta V_{cc} - \Delta V_m \quad (8)$$

The double subscripts have the following meaning: the first subscripts a and c indicate the activation losses and concentration losses respectively, and the second subscripts a and c indicate the anode (HOR electrode) and cathode (ORR electrodes) respectively. The subscript m refers to the PEM, where ohmic losses occur.

2.2. Activation losses and exchange current density

The electrochemical kinetic activity of the species reacting at the anode and cathode CLs, as in (3), produces the voltage drops ΔV_{aa} and ΔV_{ac} . Each activation voltage drop is related to the rate of charge density separation $\partial_t \rho_e$ (proton and electron creation at the anode; ∂_t represents the partial time derivative) and recombination (at the cathode), which, in steady-state conditions, are equal to the current density j_{TPB} at the TPB and can be modeled by means of the Butler-Volmer equation [16]:

$$j_{TPB} = j_{0TPBx} \left(\frac{c_{Rx}}{\bar{c}_{Rx}} e^{\alpha_x f_e \Delta V_{ax}/T} - \frac{c_{Px}}{\bar{c}_{Px}} e^{-(1-\alpha_x) f_e \Delta V_{ax}/T} \right) \quad (9)$$

where α is the transfer coefficient of each half-reaction, j_{0TPB} is its exchange current density, subscripts Rx stands for $Ra = H_2$, in the case of the anode, and for $Rc = O_2$, in the case of the cathode, and Px stands only for $Pc = H_2O$ at the cathode. Correspondingly, the ratios c/\bar{c} have the same meaning as in (6) and differ from 1 due to the concentration gradients appearing in load conditions. The structure of TPBs inside the CLs is such that the total active area A_{TPB} where j_{0TPB} is produced is much larger than the cross-section A of the device (A_{TPB}/A can be larger than 10^3). Since we are interested in modeling the cell polarization performance, we prefer to refer the exchange current density to A , by using [19]

$$j_0 = \frac{A_{TPB}}{A} j_{0TPB} \quad (10)$$

and a similar expression is used to adjust the current density of (9). The subscript x has been omitted here and in the following for the sake of simplicity. Combining (9) and (10) yields

$$j_t = j_0 \left(\frac{c_R}{\bar{c}_R} e^{\alpha f_e \Delta V_a/T} - \frac{c_P}{\bar{c}_P} e^{-(1-\alpha) f_e \Delta V_a/T} \right) \quad (11)$$

The total equivalent current density j_t appears in place of the electric current density j , to account for the effect on the overpotentials of the hydrogen crossover (Subsection 2.6). An accurate evaluation of the exchange current densities j_0 of the half-reactions is important because they strongly affect the cell performance and round-trip efficiency, according to (11). Since the effects of temperature variations had to be taken into account, the Arrhenius-like dependence of j_0 with T has been considered [20]:

$$j_0 = j_0^* e^{\frac{W_j}{R} \left(\frac{1}{T^*} - \frac{1}{T} \right)} \quad (12)$$

where W_j is an activation barrier and $j_0^* = j_0(T^*)$ with $c = \bar{c}$ (rest condition). The low operating temperature of PEMFCs and the exponential dependence of j_t on ΔV_a make activation losses the major factor responsible for the voltage drop at low current densities. Since ΔV_{ac} is typically one order of magnitude larger than ΔV_{aa} , cathode activation losses are the dominant effect at low current densities [18].

2.3. Concentration gradients

In load operation, the electric current generation at the CLs is sustained by the inflow of reagents and outflow of products, which in turn are provided by convective mass flow in the flow channels of the bipolar plates (BPs) and diffusive mass flow in the diffusion layers (DLs, Fig. 1). These mass flows produce gradients in the reagent and product concentrations and pressures, making the values c and p at the CLs different from the bulk (and inlet) values \bar{c} and \bar{p} , which affect (11) [21]. In order to model these concentration gradients ∇c , the model resorts to Fick's first law $N = -D \nabla c$, which invokes the medium diffusivity D and the gas molar flow vector N , related in turn to the current density vector j through the Faraday constant F and the charge carriers $n = 2$ for anode hydrogen and $n = 4$ for cathode oxygen:

$$j = nF N = -nF D \nabla c \quad (13)$$

Thus, the concentrations of the reacting gases at the CLs are computed as:

$$c = \bar{c} - \frac{1}{nFK} j_t \quad (14)$$

The mass transfer coefficient K

$$K = \left(\frac{d_{fc}}{Sh D_{fc}} + \frac{d_{dl}}{D_{dl}^{eff}} \right)^{-1} = \left(\frac{d_{fc}}{Sh D_{fc}} + \frac{d_{dl}}{D_{dl} \varepsilon^\tau} \right)^{-1} \quad (15)$$

takes into account both the diffusion effects within the DL laminar motion and the convective flow within the BP flow channels (Fig. 1). It depends on the flow channel hydraulic diameter d_{fc} , the DL thickness d_{dl} , their diffusivities D_{fc} and D_{dl}^{eff} , and the flow channel Sherwood number Sh [22]. The effective diffusivity D_{dl}^{eff} in the DLs is computed with the usual Bruggeman relation $D_{dl}^{eff} = D_{dl} \varepsilon^\tau$, where ε is the DL porosity and $\tau = 1.5$ (assuming $\tau = \varepsilon^{-0.5}$) [22,23]. The diffusivity dependence on temperature has been modeled as:

$$D = D^* \frac{p^*}{p} \left(\frac{T}{T^*} \right)^{2.33} \quad (16)$$

where D^* is the value of D at the temperature T^* and pressure p^* . Since our experimental setup allows us to measure pressures rather than concentrations, it is convenient to re-write (14) in terms of pressures by means of the gas law $p = cRT$, which yields for both reacting gases

$$p = \bar{p} - \frac{RT}{nFK} j_t \quad (17)$$

In this way, the effect of the temperature variation on concentration gradients can also be taken into account. The percolation of the produced liquid water at the cathodic CL also causes a pressure gradient in the water between the CL and flow channel. However, the values of p / \bar{p} significantly differ from 1 only at high current densities and high overpotentials ΔV_{ac} , namely when the second exponential in (11) vanishes. Thus they have not been considered in the model.

2.4. Concentration losses and limit conditions

Gas gradients ∇c and ∇p also produce the load term ΔE_{cl} of the Nernst equation (4), which can be written as:

$$\Delta E_{cl} = \kappa_c \frac{T}{f_e} \ln \left[\left(\frac{c_{H_2}}{\bar{c}_{H_2}} \right) \left(\frac{c_{O_2}}{\bar{c}_{O_2}} \right)^{0.5} \right] \quad (18)$$

where κ_c is a dimensionless coefficient a little larger than unity which allows us to account for secondary concentration-related effects. ΔE_{cl} is a negative variation that reduces the emf with respect to the no-load value E_{OC} and, together with the concentration effect on (11), constitutes the concentration losses which dominate the cell's performance at high current densities. Equation (18) can be rewritten as the sum of the anodic and cathodic concentration voltage drops of (8):

$$-\Delta E_{cl} = \Delta V_{ca} + \Delta V_{cc} = \kappa_{ca} \frac{T}{f_e} \ln \left(\frac{\bar{c}_{H_2}}{c_{H_2}} \right) + \kappa_{cc} \frac{T}{2f_e} \ln \left(\frac{\bar{c}_{O_2}}{c_{O_2}} \right) \quad (19)$$

These two terms provide the anodic and cathodic current density limits, namely the theoretical values of the current densities which cause the CL concentrations and pressures to vanish and the half-reaction stop, in a starvation condition:

$$\begin{aligned} j_{La} &= n_{H_2} F K_a \bar{c}_{H_2} = f_e K_a \bar{p}_{H_2} / T \\ j_{Lc} &= n_{O_2} F K_c \bar{c}_{O_2} = 2f_e K_c \bar{p}_{O_2} / T \end{aligned} \quad (20)$$

Since the smaller limit current density occurs at the cathode, due to the lower diffusivity of oxygen compared to hydrogen, j_{Lc} constitutes the device's current density limit.

2.5. PEM ohmic losses

Nafion®, which consists of polytetrafluoroethylene (PTFE) backbones bearing perfluoroetheral side chains terminated with sulfonic acid groups [24], is the most-used material for PEM, because it exhibits an excellent behavior as a protonic ohmic conductor when properly hydrated. ΔV_m of (8) is thus:

$$\Delta V_m = \frac{d_m}{\gamma} j \quad (21)$$

where d_m is the PEM thickness. The conductivity γ depends on temperature and hydration, namely the ratio $\lambda = c_w/c_{sa}$ between water and sulfonic acid concentrations, that can vary in the range 0–22 for typical perfluorinated proton-conducting membranes based on Nafion®

$$\gamma(\lambda) = \gamma_o(T) B \lambda \quad (22)$$

The linear dependence on λ via the dimensionless coefficient B is the adaptation of an empirical model [25] aimed at avoiding a negative value of γ at lower λ . The temperature dependence is expressed according to the Vogel-Tamman-Fulcher model [26–28]:

$$\gamma_o(T) = A_0 T^{-0.5} e^{\frac{W_m}{R(T_g - T)}} \quad (23)$$

where $A_0 = 0.048 \text{ K}^{0.5} \text{ S/cm}$, $T_g = 157 \text{ K}$ is the glass transition temperature, and $W_m = 1.86 \text{ kJ/mol}$ is the activation barrier. Although λ varies along the PEM's thickness d_m according to back-diffusion and electro-osmotic drag [29], the average between the PEM boundary values λ_a and λ_c (i.e. at the CLs) has been used in (22), consistently with a linear profile between λ_a and λ_c . These values depend on the water activities a_{wa} and a_{wc} of the reacting gases at the CLs, and are computed with the empirical polynomial [25]:

$$\lambda = \begin{cases} 0.043 + 17.81 a_w - 39.85 a_w^2 + 36.0 a_w^3 & 0 \leq a_w \leq 1 \\ 14 + 1.4(a_w - 1) & 1 \leq a_w \leq 3 \end{cases} \quad (24)$$

The water activity is the relative humidity expressed in absolute terms and is computed from the water vapor partial pressure p_w and the water vapor saturation pressure p_{ws} :

$$a_w = \frac{RH}{100} = \frac{p_w}{p_{ws}(T)} \quad (25)$$

with [18]:

$$p_{ws} = 10^{(-2.1794 + 0.2953T - 9.1837 \cdot 10^{-5} T^2 + 1.4454 \cdot 10^{-7} T^3)} \quad (26)$$

Since the setup used in collecting the experimental data for the stochastic identification assures high gas flow rates, the values p_{wa} and p_{wc} of the partial pressure at the CLs have been assumed equal to the values in the BP flow channels. Consistently, the gas bulk pressures and concentrations \bar{c} and \bar{p} used in the previous equations are derived from the total bulk pressures p_I at both anode (hydrogen) and cathode (oxygen) BPs:

$$\begin{aligned} \bar{p}_a &= (p_{Ia} - a_{wa} p_{wsa}) \\ \bar{p}_c &= g (p_{Ic} - a_{wc} p_{wsc}) \end{aligned} \quad (27)$$

$$\begin{aligned} \bar{c}_a &= \frac{1}{RT} (p_{Ia} - a_{wa} p_{wsa}) \\ \bar{c}_c &= \frac{g}{RT} (p_{Ic} - a_{wc} p_{wsc}) \end{aligned} \quad (28)$$

where $g = 0.21$ if the cathode is fed with air and $g = 1$ in the case of pure oxygen.

2.6. Hydrogen crossover

Fuel crossover consists of hydrogen that does not react at the anode but migrates through the PEM to react at the cathode directly with oxygen, without producing electric power. This is a major side-effect that affects the FC performance and efficiency and depends on two causes, diffusion and electro-osmotic drag. Hydrogen mass flow and its two contributions have been modeled as equivalent current densities, according to (13)

$$j_{co} = j_{cod} + j_{coe} \quad (29)$$

Diffusive crossover depends on the hydrogen concentration gradient inside the PEM and its equivalent j_{cod} can be modeled with Fick's first law:

$$j_{cod} = \frac{nF D_{mH_2}}{d_m} c_{H_2} \quad (30)$$

where c_{H_2} is the hydrogen concentration at the anodic CL, as in (14) and constitutes the gradient itself, assuming zero concentration at the cathodic CL (namely, a complete reaction of all the hydrogen arriving here). D_{mH_2} is the hydrogen diffusivity inside the PEM, whose dependence on temperature has been modeled with an Arrhenius-like equation:

$$D_{mH_2} = D_{mH_2}^* e^{-\frac{W_{mH_2}}{R} \left(\frac{1}{T^*} - \frac{1}{T} \right)} \quad (31)$$

where W_{mH_2} is an activation barrier and $D_{mH_2}^* = D_{mH_2}(T^*)$. Electro-osmotic drag consists of hydrogen drawn by protons while migrating from anode to cathode, namely producing the electric current density j . It accounts for crossover effects at low c_{H_2} values, i.e. when j approaches the limit current density j_L . Its equivalent j_{coe} is modeled as [30]:

$$j_{coe} = n\zeta \lambda j \quad (32)$$

where ζ is a dimensionless electro-osmotic drag coefficient. Eq. (32) takes into account an intensifying effect with hydration, as happens with water electro-osmotic drag. The resulting equivalent crossover current density depends on hydrogen concentration, hydration, and PEM protonic current density:

$$j_{co} = \frac{nF D_{mH_2}}{d_m} c_{H_2} + n\zeta \lambda j \quad (33)$$

Crossover hydrogen reacts at the cathode, increasing the activation overpotential ΔV_{ac} , mass flow in both DLs and their concentration losses ΔV_{ca} and ΔV_{cc} . Consequently, in (11), (14), and (17), the total equivalent current density j_t is considered:

$$j_t = j + j_{co} \quad (34)$$

Crossover hydrogen is the main cause of the difference between the open circuit emf E_{OC} of (7) and the observed OCV $V(0)$ [31]. It also causes a loss of stored energy that reduces round-trip efficiency. Also oxygen diffuses through the PEM, but, since its diffusivity is much lower than hydrogen [23], it has been neglected in this model.

2.7. Thermal gradient

The dissipations occurring inside the cell produce thermal gradients which affect the temperature-dependent parameters. The model takes into account such dependences by considering the dissipative effects occurring in the CLs and in the PEM. The thermodynamic heat generation per unit area (Peltier heating) related to the formation of the reversible voltage E of (4) in load condition is written as:

$$P_p = -N(\Delta\hat{h} - \Delta\hat{g}) = -j \frac{T\Delta\hat{S}}{nF} \quad (35)$$

where $\Delta\hat{h}(T)$ and $\Delta\hat{g}(T)$ are the molar reaction enthalpy and Gibbs' energy. The losses per unit area related to the electrochemical kinetic activity at the anode and cathode CLs are given as:

$$P_a = j \Delta V_a(j) \quad (36)$$

Finally, the joule losses per unit area in the PEM are written as:

$$P_m = \frac{d_m}{\gamma} j^2 \quad (37)$$

so that inside the cell thickness the dissipated power per unit area is:

$$P_{diss} = j \left[-\frac{T\Delta\hat{S}}{nF} + \Delta V_a(j) \right] + \frac{d_m}{\gamma} j^2 \quad (38)$$

Heat transport inside the cell depends on conduction, diffusion, convection and possibly radiation and must take into account the thermal capacity in dynamic conditions [18,22]. The temperature distribution can then be obtained by 3D integration of the resulting partial differential equations. However, for the aim of this model, a simpler evaluation is sufficient, suitable to provide an accurate enough estimation of the mean temperature T inside the cell with respect to the room and gas inlet temperature T_r , so the following equation has been used:

$$T = T_r + k_t P_{diss} \quad (39)$$

where k_t is a global thermal exchange coefficient. In order to avoid further major numerical complication involving convergence issues, a second order polynomial approximation of (38) has been adopted, which allows us to re-formulate (39) as

$$T = T_r + k_{t1} j + k_{t2} j^2 \quad (40)$$

where k_{t1} and k_{t2} are parameters to be identified within the stochastic search.

2.8. Model numerical implementation

In the numerical implementation of the model, consistent analytical expressions for all the input/output relationships have been imposed, while avoiding the introduction of approximations. With this aim, the numerical model uses the electric current density j as the independent variable to compute all voltage terms of (8). In order to deal with the non-invertible Butler-Volmer equation (11), a tabulated dataset approach has been used, which allows us to obtain the activation losses from the current density by resampling.

3. Stochastic optimization

A number of nonlinear deterministic optimization methods have been applied to PEMFCs in the last decade, proving successful in dealing with specific tasks. Least squares methods have been applied to the estimation of single material parameters (e.g. membrane conductivity, exchange current densities, oxygen diffusion coefficients as well as parameters evolution under degradation events and semi-empirical parameters [32–34]). Support vector machine (SVM) approaches, i.e. learning algorithms that analyze data and recognize patterns, have been used for predictive control and real-time diagnostics [35–37]. The Gradient method has been exploited in the search for optimal designs and parameters evolution, such as cathode configuration optimization, geometric optimization, and flow field serpentine optimization [38–41]. A review of deterministic optimization methods used for identification problems in PEMFCs is given in [42]. These researches show that such methods can be effective and fast in solving specific problems. However, they suffer from some drawbacks, e.g. they may lack flexibility to handle arbitrary constraints, are sensitive to noise, may require function derivatives and are prone to remain trapped in local minima.

Stochastic optimization methods are very appealing in dealing with these problems, because they can overcome the limitations of deterministic methods. In fact, the strong nonlinearity of FC models yields non-convex formulations of the identification problems. Stochastic optimizers are intrinsically tailored for escaping the resulting local minima, unlike deterministic optimizers. Moreover, stochastic methods can simultaneously deal with the several parameters used in FC characterization and modeling, thanks to their metaheuristic nature (they are the most common of the metaheuristic techniques) and can also deal with non-differentiable optimization problems. Stochastic methods have also been introduced in the analyses of FCs in the last decade and their use has been strongly increasing in recent years. Several stochastic methods have been used, *i.e.* genetic algorithms (GA) [413,44], Particle Swarm Optimization (PSO) [45,46] and Differential Evolution (DE) [47,48], just to name the most well known. Such iterative methods typically work with populations of candidate solutions (*i.e.*, of tentative x of (1) which iteratively aim at x_0). They use random variables, which can be introduced in different points within the optimization algorithm, and the type of randomness may be trimmed to the problem at hand in order to achieve the best performance. Although the convergence to the global optimum is guaranteed only asymptotically, there is abundant numerical evidence that very good solutions can be obtained for most problems without requiring specific and detailed model assumptions. Such methods provide noise robustness, *i.e.* reduced sensitivity to modeling and data errors [49]. On the other hand, stochastic methods are computationally very expensive (*i.e.* they require large CPU and computation time), but are also usually intrinsically suitable for parallel computation, that can be performed in high-performance computers. In consideration of their high computational costs, a crucial feature of FC stationary models is that the latter avoid partial differential equations thus resulting in numerical formulations with relatively low computational costs, which can be affordably used in stochastic routines. A large number of stochastic optimization methods have been developed, among which those best fitted to a specific task can be selected. The solution strategy can make use of a single method, as well as of combinations of them, in order to exploit and merge their specific capabilities. This is the strategy we have developed, based on particle swarm optimization (PSO) and differential evolution (DE).

3.1. Particle swarm optimization – PSO

PSO is inspired by the social behavior of birds. After early studies on its mathematical modeling by biologist Craig Reynolds, Russel Eberhart and James Kennedy recognized the suitability of this technique for optimization and developed PSO in 1995 [50].

The algorithm makes use of a population of *particles*, whose *positions* in the search space A are candidate solutions, all of which at every iteration change their positions (*i.e.*, each candidate solution is replaced by another candidate solution) through *velocities*, in search of positions which provide good values of the fitness function f , similarly to birds and fish searching for food (Fig. 2-a). At each iteration the *personal best* of each particle and the *global best* of the whole population is recomputed and updated. Such information is shared among particles, in the same way that birds and fish exchange information by acoustic and optical means. Randomness is introduced at every iteration in the individual velocity, while taking into account both personal and global performance. In algorithmic terms, the main steps of a PSO are (Fig. 2-b):

- 1) PSO is initialized by providing a population of n particles with random positions x_i and velocities v_i in A .
- 2) Each particle's fitness $f(x_i)$ is evaluated and, if improved, the personal best is updated $p_i = x_i$;

$$p_i(t) = \begin{cases} p_i(t-1) & \text{if } f(x_i) \geq f(p_i(t-1)) \\ x_i & \text{if } f(x_i) < f(p_i(t-1)) \end{cases} \quad (41)$$

and the new global best p_g among the p_i of the whole population is identified.

- 3) Velocity v_i and position x_i of each particle are updated according to:

$$\begin{aligned}
v_i(t+1) &= w v_i(t) + c_1 r_1 [p_i(t) - x_i(t)] + c_2 r_2 [p_g(t) - x_i(t)] \\
x_i(t+1) &= x_i(t) + \Delta t v_i(t+1)
\end{aligned}
\tag{42}$$

and a foraging strategy consisting in a velocity limitation is also adopted:

$$v_i(t+1) = \begin{cases} v_{\max} & \text{if } v_i(t+1) > v_{\max} \\ -v_{\max} & \text{if } v_i(t+1) < -v_{\max} \\ v_i(t+1) & \text{else} \end{cases}
\tag{43}$$

4) A convergence test is performed and if not satisfied, the control goes back to step 2); else the algorithm stops.

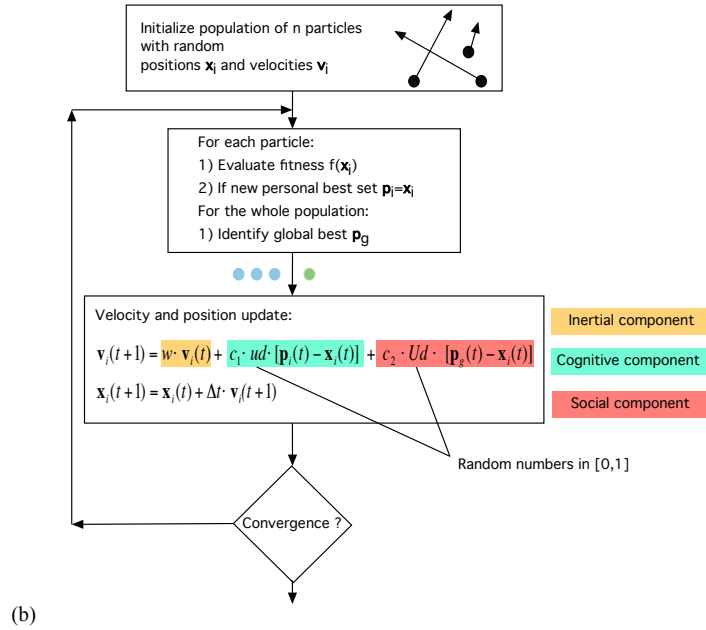
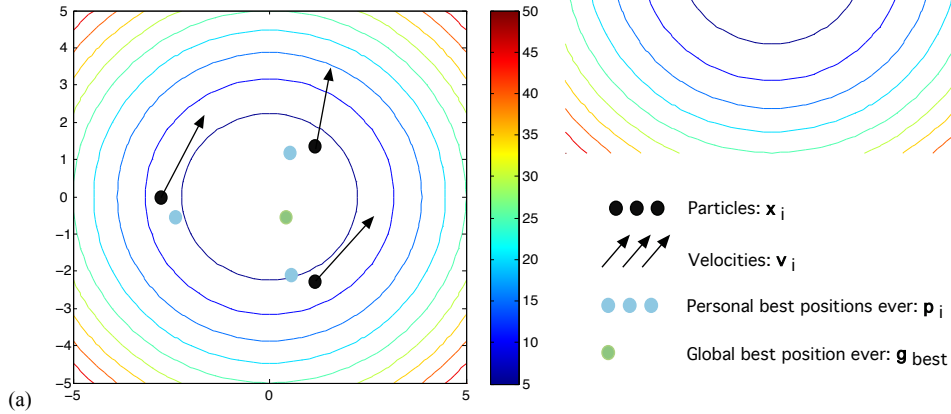


Fig. 2. PSO: (a) scheme of concepts and (b) algorithm.

The number of particles n , the inertia w (weight) and the learning factors c_1 , c_2 are to be tailored by the operator to the optimization problem at hand. The weight w (i.e. the inertia) is a positive value and the larger it is the better the global search, while the smaller it is the better the local search. Consistently, a linearly decreasing $w(t)$ provides better overall performance, with typical boundaries $w_{\max} = 0.9$ and $w_{\min} = 0.4$. The learning factors c_1 , c_2 are usually set in order of 2. r_1 , r_2 are two randomly generated numbers in the range (0,1). The three terms forming v_i in (42) take into account inertia, the cognition (memory) of each particle,

and the social behavior (exchange of information among particles), respectively. A large number of iterations is usually needed, as large as $t = 20,000$ and more, which is impracticable with computationally heavy models. The PSO algorithm intrinsically favors, with respect to other stochastic algorithms, explorations of the search space A , i.e. the search for the global optimum. This desirable feature, however, is obtained at the cost of lower computational efficiency with respect to other competing methods.

3.2. Differential Evolution – DE

DE was developed in 1995 by Rainer Storn and Kenneth Price [51,52]. It uses a population of *agents* which move in the search space A according to simple formulae combining the agents' positions (candidate solutions), and new positions are accepted if their fitness improves (Fig. 3-a).

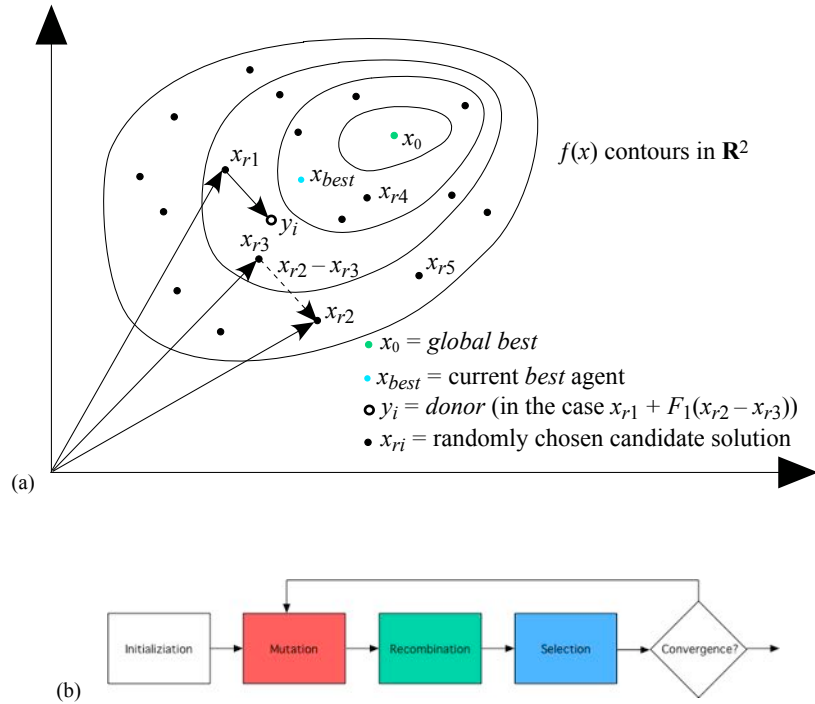


Fig. 3. DE: (a) Scheme of Scheme of concepts ; (b) algorithm.

The algorithm iteration consists of three steps (Fig. 3-b) and the iterations proceed as follows:

- 1) DE is initialized by providing a population of n agents with random positions x_i in A and their fitness $f(x_i)$ is evaluated.
- 2) The *mutation* step allows the search macro-space to be expanded by adding difference vector(s) to all agents, according to specifically tailored schemes. Some examples are:

$$\begin{aligned}
 y_i &= x_{r1} + F_1(x_{r2} - x_{r3}) \\
 y_i &= x_{best} + F_1(x_{r2} - x_{r3}) \\
 y_i &= x_{r1} + F_1(x_{r2} - x_{r3} + x_{r4} - x_{r5}) \\
 y_i &= x_{best} + F_1(x_{r2} - x_{r3} + x_{r4} - x_{r5}) \\
 y_i &= x_{r1} + F_1(x_{r2} - x_{r3}) + F_2(x_{best} - x_{r1}) \\
 y_i &= x_i + F_1(x_{r2} - x_{r3}) + F_2(x_{best} - x_i)
 \end{aligned} \tag{44}$$

- 3) The *recombination* step recovers the features of previously successful individuals (candidate solutions):

$$u_{ij} = \begin{cases} y_{ij} & \text{if } R_{ij} \leq CR \text{ or } j = I_r \\ x_{ij} & \text{else} \end{cases} \tag{45}$$

- 4) The *selection* step allows selection of the best performing candidate solutions, mimicking a survival-of-the-fittest. A greedy scheme is used, that enables a fast convergence:

$$x_i^{k+1} = \begin{cases} u_i^k & \text{if } f(u_i^k) \leq f(x_i^k) \\ x_i^k & \text{else} \end{cases} \quad (46)$$

- 5) A convergence test is performed and if not satisfied, the control goes back to point 2); else the algorithm stops.

In (44), *donors* y_i are proposed changes in agent positions, computed from randomly chosen candidate solutions x_{r1}, \dots, x_{r5} and the current best *agent* x_{best} , making use of operator-chosen parameters F_1 and F_2 (mutation factors). In (45), u_{ij} is the j -th component of the trial agent u_i , that is a tentative new candidate solution, R_{ij} the corresponding uniformly distributed random real number in the range 0–1, CR is the operator-chosen crossover ratio, and I_r is a random integer in the range 1– n (with n the dimension of \mathbf{R}^n). In (46), the tentative new candidate solutions are accepted if they improve the agent fitness. A DE algorithm intrinsically favors exploitation, i.e. fast convergence toward a minimum, because of the greedy scheme (46), but the solution can remain trapped in local minima.

4. Tailoring the stochastic search

4.1. Hybrid stochastic strategy

In order to take advantage of the capability of PSO as regards exploration and DE as regards exploitation, we developed a hybrid optimization scheme that uses alternatively both of them at each iteration, according to the scheme of Fig. 4a, with each algorithm utilizing its own population of candidate solutions. As shown later on, tests proved that this hybrid scheme is capable of avoiding local minima and rapidly converging to what is reasonably the global minimum. Fig. 4b shows that both populations cooperate in the identification of the minimum and Table 1 presents a comparison among the results obtained with the hybrid algorithm and with the PSO and DE alone.

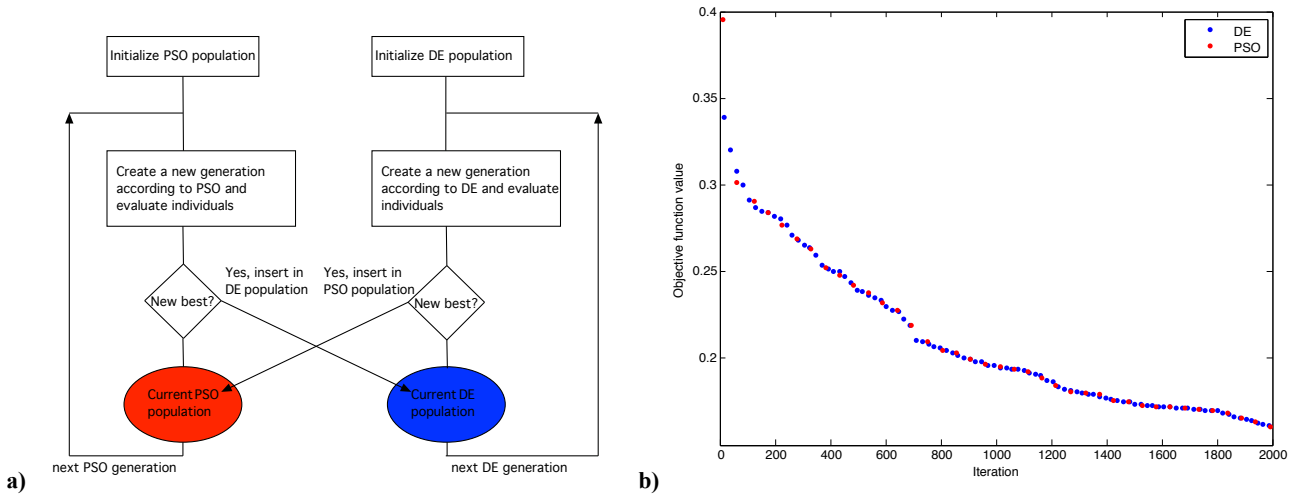


Fig. 4. Hybrid scheme based on the combination of PSO and DE. a) flowchart, b) objective function improvement due to DE and PSO for the polarization curve at $T_r = 40^\circ\text{C}$, $p_{bp} = 15$ psig, and $RH = 100\%$.

Table 1: Effect of the specific optimization algorithm. Statistics collected over 50 runs, performed on an experimental polarization curve at $T_r = 40^\circ\text{C}$, $p_{bp} = 15$ psig, and $RH = 100\%$. Bold indicates best value in the column. The objective function f is given in (47).

	Best f	Avg. f	Worst f	Std. Dev. f
<i>DE</i>	218.1E-3	277.0E-3	388.2E-3	41.8E-3
<i>PSO</i>	278.1E-3	356.9E-3	536.2E-3	55.7E-3
<i>Hybrid PSO+DE</i>	153.5E-3	228.4E-3	359.7E-3	40.5E-3

4.2. Fitness function

The fitness function f of (1) that has to be minimize is built on the differences between the computed $V_{\text{mod}}(j)$ and measured $V_{\text{exp}}(j)$ voltages along the cell polarization curves. $V_{\text{mod}}(j)$ are provided by (19), based on the model described in Section 2, while $V_{\text{exp}}(j)$ are obtained from an experimental set-up that assures controlled cell temperature, gas pressures and relative humidity, as described in Section 5. Several fitness functions f of (1) can be defined, e.g. functions f_1 and f_2 in (47), and in principle all can provide a perfect fit between the experimental data and model outputs when minimized, but they have different “landscapes” that make the minimization process harder or easier. Numerical experiments have shown that the best results in terms of computational efficiency and the stability of the obtained results over several runs are obtained by the following fitness function:

$$\begin{aligned}
 f(x) &= 0.5f_1(x) + 0.5f_2(x) \\
 x &= V_{\text{mod}} - V_{\text{exp}} \\
 f_1 &= \max |x_i| \\
 f_2 &= \sqrt{\sum x_i^2}
 \end{aligned} \tag{47}$$

Table 2 shows a comparison between different choices for f . It can be noted that constructing an objective function which is a weighted average between the maximum (f_1) and RMS (f_2) deviation between model output and experimental data provides better final RMS approximation than using f_2 which uses the RMS value only.

Table 2: Effect of the choice of objective function f . Statistics collected over 50 runs of the hybrid PSO-DE algorithm, performed on an experimental polarization curve at $T_r = 40^\circ\text{C}$, $p_{bp} = 15$ psig, and $RH = 100\%$. Bold indicates best value in the column.

	Best f_1	Avg. f_1	Worst f_1	Std. Dev. f_1	Best f_2	Avg. f_2	Worst f_2	Std. Dev. f_2
$f = f_1$ of (47)	21.5E-3	32.95E-3	41.3E-3	5.0E-3	459.2E-3	722.8E-3	941.2E-3	129.6E-3
$f = f_2$ of (47)	20.8E-3	75.5E-3	94.9E-3	21.6E-3	294.3E-3	452.7E-3	861.1E-3	120.5E-3
$f = 0.5f_1 + 0.5f_2$	19.9E-3	45.3E-3	78.8E-3	21.5E-3	283.2E-3	411.4E-3	675.2E-3	91.7E-3

4.3. Anti-duality strategies

Duality, namely multiple solutions x achieving the same accuracy in minimizing f , is a major problem arising when the number of unknowns is large and the non-linear problem is weakly constrained. In order to overcome it, a strategy has been adopted that consists in splitting the search into more identification sub-problems, each having a lower number of unknowns. A number of techniques are available with which to take advantage of this approach and they basically rely on isolating a group of equations, which can yield some of the unknowns, some having already been applied to fuel-cell analyses [53,54]. One example is the current switch method [55,56]. Our strategy consists in a three-phase approach:

- 1) Preprocessing: in the first phase the PEMFC open circuit operation is analyzed;
- 2) Core processing: in the second phase the working points in load condition along the polarization curves are selectively used according to the locally dominant loss effect (i.e. activation losses, ohmic losses, and concentration losses);

- 3) Postprocessing: in the third phase, the parameters identified in the previous two phases are used to determine the remaining unknowns and validate the previous ones.

4.4. Preprocessing: OCV analyses

Tafel's slope method allows us to extract information from working points at low current density j along the polarization curve. For large enough ΔV_a (say >100 mV), the backward current density of the Butler-Volmer equation (11) is negligible compared with the forward one (roughly by a factor of 100), so that the equation can be reversed as

$$\ln j_t = -\ln j_0 + \ln \frac{\bar{c}_R}{c_R} + \frac{\alpha f}{T} \Delta V_a \quad (48)$$

On the other hand, if the current density j is not too high (typically 100–150 mA) the activation voltage drops, and in particular the cathodic one ΔV_{ac} , are much higher than the concentration and membrane voltage drops ΔV_c and ΔV_m , so we can assume that $\Delta V_{ac} \cong \Delta V = E_{OC} - V(j)$. Consistently with (19), in such a low current density condition we can also assume the CL gas concentrations equal to the bulk values, $\bar{c} \cong c$, so that Tafel's approximation holds [23]:

$$\ln j_t = -\ln j_{0c} + \frac{\alpha_c f}{T} (E_{OC} - V) \quad (49)$$

This equation allows us to extract the dominant (cathodic) exchange current density j_{0c} and its transfer coefficient α_c from properly selected experimental data j and V , at known bulk gas pressures p_I and temperature T , E_{OC} being computed by means of (7). Furthermore, extrapolating $V(j)$ data at very low j provides the OCV $V(0)$, which differs from the open circuit fem E_{OC} because of hydrogen crossover, represented by j_{cod} of (30). By using j_{0c} , α_c , and $\Delta V(0)$ in (11), $j_t = j_{cod}$ at $j = 0$ is obtained, that allows to compute D_{mH_2} . Repeating the computation at different temperatures provides data for a best-fit determination of W_{mH_2} of (31). In short, this phase allows us to identify $\alpha_c, j_{0c}, W_i, j_{cod}, D_{mH_2}, W_{mH_2}$.

4.5. Core processing: selective variable separation

A straightforward use of a stochastic optimizer with a large number of unknowns (n of \mathbf{R}^n) can result in duality with unrealistic results, because the objective function may be much more sensitive to some unknowns than to others causing the latter to vanish. This behavior has emerged in experimenting with the present application of stochastic optimizers, in which we found that the parameters related to the activation losses and to the concentration losses, which are strongly non-linear, prevail over the ohmic losses, which are linear at given hydration and temperature, and their identified values tend to vanish. On the other hand, we can use this non-linearity to our advantage. Our strategy consists in exploiting the characteristic behavior of FCs, by selectively using the typical three portions of their polarization curves. Thus we used the experimental data at low current density to identify the parameters related with the activation losses, which dominate the polarization curve in such working condition. Then we used the experimental data at high current density to identify the parameters related with the concentration losses, which dominate the corresponding portion of the polarization curve. Finally, we used the experimental data at intermediate current density to identify the parameters related with the ohmic losses.

4.6. Postprocessing: temperature correlations

In the final phase we used the parameters identified from the experimental data acquired at different temperatures for fitting pertinent correlation parameters, such as the activation barriers.

4.7. Computational complexity

The numerical model described in Section 2 allows to evaluate a single polarization curve in less than 0.1 seconds on standard PC hardware so that the complete set of 12 experimental curves described in Section 5 were reconstructed in approximately 1 second (we used a Mac iBook with a 2.6 GHz i7 Intel processor and a 1.6 GHz 8 GB DDR3 memory). A typical optimization run

requires the evaluation of some thousands of models, the exact number depending on algorithmic settings and convergence criteria, and lasted between 1 and 3 hours in our case. Speedups of one order of magnitude, i.e. maximum total run times in the order of 20 minutes can be easily achieved through parallelization of the objective function evaluation, which is not currently implemented in our algorithm. A high performance machine with parallelized computing can allow to implement more sophisticated PDE models describing the spatial distribution and time evolution of the physical quantities inside the cell, which can underpin a keener optimization processes.

5. Experimental data

5.1. Test PEMFC preparation

The experiments were carried out on a membrane-electrode assembly (MEA) fabricated in accordance with the procedure reported in [57]. Briefly, a Nafion117™ membrane procured from Ion Power was activated as described in [58] and subsequently dried overnight at room temperature. Two identical electrode inks were prepared, comprising a Pt-black electrocatalyst (BASF C6-100) and Nafion® ionomer (Ion Power 5 wt% solution), which were suspended in a water/isopropanol 1/10 w/w solution. Each electrode ink was thoroughly homogenized with a probe sonicator and subsequently painted on a square 2×2 cm gas diffusion substrate (GDS1120 carbon paper with a thickness of 184 microns, obtained from Ballard Material Products); solvents were removed under an IR lamp. The resulting gas diffusion electrodes were hot-pressed onto the dried Nafion117™ membrane, yielding an MEA. The loading of Pt in each catalyst layer was 4 mg cm^{-2} . The electrochemically active surface area A_{TPB} referred to the Pt loading was $19.4 \text{ m}^2 \text{ g}_{\text{Pt}}^{-1}$, as determined *in situ* with the “driven cell” method [4,5,9].

5.2. Experimental set-up

The MEA experimental data were acquired on a high-performance dedicated test station consisting of a single cell fixture, a test chamber, a gas supply system, an electronic load and an acquisition system. The test chamber (Fig. 5) allowed the experiments to be run under a controlled room temperature. The reactants were humidified, achieving a dew point up to 100°C ; their pressures were controlled by means of back-pressure valves, which allowed a back pressure of up to 100 psig to be achieved. The gas supply system provided highly pure reactants. 99.9999% pure H_2 was produced by a hydrogen generator (Strumenti Scientifici Cinel); pure O_2 was obtained from a conventional high-pressure tank (Alphagaz® 1 grade, Air Liquide); air was drawn from a conventional high-pressure tank. The flow rate of H_2 could be varied in the 10–1000 sccm range; in the case of both pure oxygen and air, the flow rate could be varied in the 20–2000 sccm range. The electronic load allowed exploration of the polarization curve from near open-circuit to almost short-circuit (i.e. near the cell limit current density).

Experiments were carried out in the following physical conditions:

- 1) room temperature: $T_r = 40\text{--}60\text{--}85^\circ\text{C}$,
- 2) total gas back pressure: $p_{bp} = 15\text{--}65$ psig (205–550 kPa),
- 3) inlet gas relative humidity: $RH = 50\text{--}100\%$,

It is pointed out that: (i) the flow rates chosen for the experiments corresponded to very high stoichiometric factors (equal to *ca.* 30 or higher); (ii) the active area A of the single cell was very small; (iii) the water provided by the reactant streams was always much more than that produced by the cell upon operation; and (iv) in the experimental setup, the MEA was placed in a very massive, temperature-controlled single fuel cell fixture (Fig. 5). In these conditions, it could be assumed that: (i) the controlled back pressures p_{bp} at each electrode are equal to the total bulk pressures p_I used in the model; (ii) liquid water does not condense in the PEMFC during operation, preventing complications arising from two-phase liquid saturation; (iii) PEMFC hydration is controlled for the most part by the reactant streams, allowing to neglect issues arising from water transport; and (iv) the amount of heat produced by the cell (on the order of a few watts) was effectively removed by the circulating fluids and was insufficient to affect

significantly the temperature of the system, thus preventing heat buildups. The above considerations ensure the applicability of the proposed stationary zero-dimensional multiphysics performance model to the analysis of the experimental polarization curves.

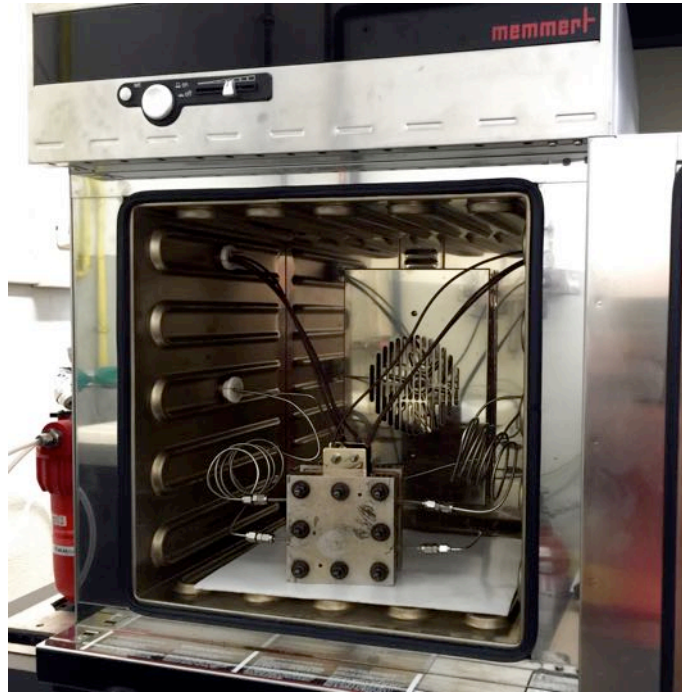


Fig. 5. Test chamber used for collecting the experimental polarization curves under controlled conditions

6. Results

In the following, we present the result of multi-parameter identification obtained by means of the PEMFC multiphysics performance model coupled with the stochastic algorithm described in sections 4 and 5, respectively. The experimental data used in the identification were obtained with the experimental set-up described in section 6 and consisted of 12 polarization curves, each obtained in a different physical condition as regards room temperature T_r , total gas back pressure p_{bp} and gas relative humidity RH (i.e. water activity a_w).

6.1. Pre-identification – Tafel slope

In this phase, the model parameters $\alpha_c, j_{0c}, W_j, j_{cod}, D_{mH_2}, W_{mH_2}$ were pre-identified. In order to perform the preprocessing algorithm as described in subsection 5.4, proper sub-sets of each experimental polarization curve were used, typically with j ranging from 2.5 mAcm^{-2} to $25\text{--}38 \text{ mAcm}^{-2}$. As an example, some values obtained at $T_r = 40\text{--}85^\circ\text{C}$, $p_{bp} = 15 \text{ psig}$, $RH = 100\%$ are shown in Table 3. Changing these conditions, consistent values were obtained, e.g. $\alpha_c = 0.59$ at $T_r = 40\text{--}85^\circ\text{C}$, $p_{bp} = 65 \text{ psig}$, $RH = 100\%$. These values were used as reasonable starting values for the stochastic optimization performed in the core identification phase.

Table 3: Some model parameters identified in the pre-processing phase.

	α_c	j_{0c} μAcm^{-2}	J_{cod} mAcm^{-2}	D_{mH_2} $\text{cm}^2 \text{s}^{-1}$	W_{mH_2} J mol^{-1}
$T = 40^\circ\text{C}$ $p_{bp} = 15 \text{ psig}$ $RH = 100\%$	0.36	3.16	0.23	0.17	576
$T = 85^\circ\text{C}$ $p_{pb} = 15 \text{ psig}$ $RH = 100\%$	0.38	4.85	0.27	0.42	576

6.2. Core identification – Hybrid selective stochastic method

This phase allowed us to identify the model parameters α_c , j_{0c} , W_{jc} , J_{cod} , K_c , K_a , κ_{ca} , κ_{cc} , B , ζ , k_{t1} , k_{t2} , by means of the hybrid PSO-DE optimization algorithm presented in section 5. The polarization curve of a fuel cell presents three distinct sections in which different loss effects dominate the cell behavior, namely: i) the activation losses at low current density, ii) the ohmic losses at intermediate current density, and iii) the concentration losses at high current density. This feature was exploited in order to minimize the duplicity problem, by selectively operating the hybrid optimization algorithm in four steps.

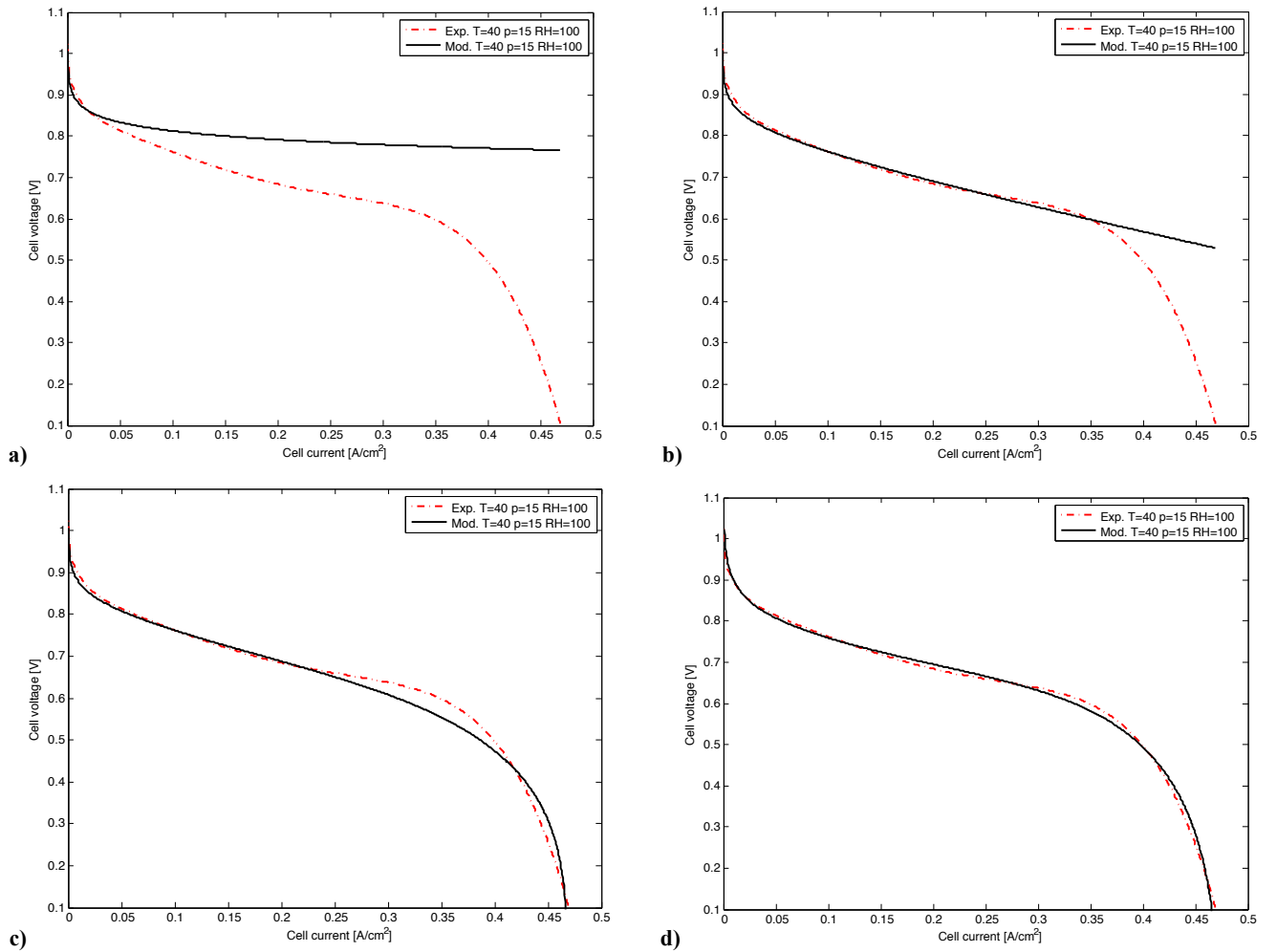


Fig. 6. Core identification of hybrid PSO-DE algorithm, performed on an experimental polarization curve at $T_r = 40^\circ\text{C}$, $p_{bp} = 15 \text{ psig}$, and $RH = 100\%$.

a) Step 1 = low current density and activation-related parameters. b) Step 2 = intermediate current density and ohmic-related parameters.

c) Step 3 = high current density and concentration parameters. d) Step 4 = trimming of all parameters on the whole polarization curve.

Step 1: Identification of activation loss parameters

The algorithm searched for the parameters related to the activation losses by using the initial part of the polarization curve in the fitness function f of (47) and assuming that in this part of the curve the concentration ratios in (11) can be considered equal to one, namely that the concentration of the reactants at the CLs is the same as in the bulk. The parameters identified were: α_c , j_{0c} , W_{jc} , j_{cod} . Fig. 6-a shows the result of step 1 for the experimental curve at $T_r = 40^\circ\text{C}$, $p_{bp} = 15$ psig, $RH = 100\%$.

Step 2: Identification of membrane loss parameters

The algorithm retained the parameters identified in step 1 and searched for the parameters related to the ohmic losses in the membrane by using the polarization curve at intermediate current density the fitness function (47). The parameter identified was B . Fig. 6-b shows the result of step 2.

Step 3: Identification of concentration loss parameters

The algorithm retained the parameters identified in steps 1 and 2 and searched for the parameters related to the concentration losses by using the complete polarization curve in the fitness function (47). The parameters identified were: K_a , K_c , κ_{ca} , κ_{cc} . Fig. 6-c shows the result of step 3.

Step 4: Combined optimization of all parameters

Since the initial guess can significantly affect the performance of any stochastic optimization, a final search was performed, in which the algorithm executed a post-optimization which rearranged all parameters starting from their already identified values. In this step parameters k_{i1} , k_{i2} and ζ were also added to the problem degrees of freedom. This final step was actually found to further improve the fit. Fig. 6-d shows the result of step 4.

The core identification based on the selective hybrid PSO-DE algorithm can be carried out not only on single curves, as shown above, but also on several curves at once. This approach was used to obtain the polarization curves shown in Fig. 7.

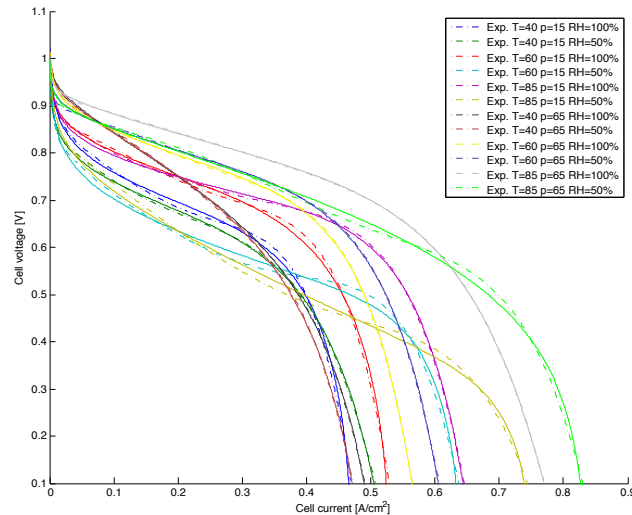


Fig. 7. Result of the core identification by means of the selective hybrid PSO-DE algorithm run simultaneously on all polarization curves.

Dashed lines: experimental, continuous lines: optimized models.

6.3. Postprocessing

Since the optimization procedure is stochastic, different runs produce different results which may or may not give a satisfactory fitting of the experimental curve, calling for a critical analysis of the optimization outputs. Fig. 8-a highlights this effect, by showing the seven best optimized parameter combinations obtained after 20 different runs of the procedure. The corresponding polarization curves are shown in Fig. 8-b. It can be seen that quite good results can be obtained for several values of most parameters, although the correspondence between the model and experiment is more sensitive to some parameters than to others, as shown by their tighter clustering. Table 4 reports the values of the parameters α_c , j_{0c} , W_{jc} , j_{cod} , K_c , K_a , κ_{ca} , κ_{cc} , B , ζ , k_{t1} , k_{t2} identified with the hybrid selective stochastic method in the core phase.

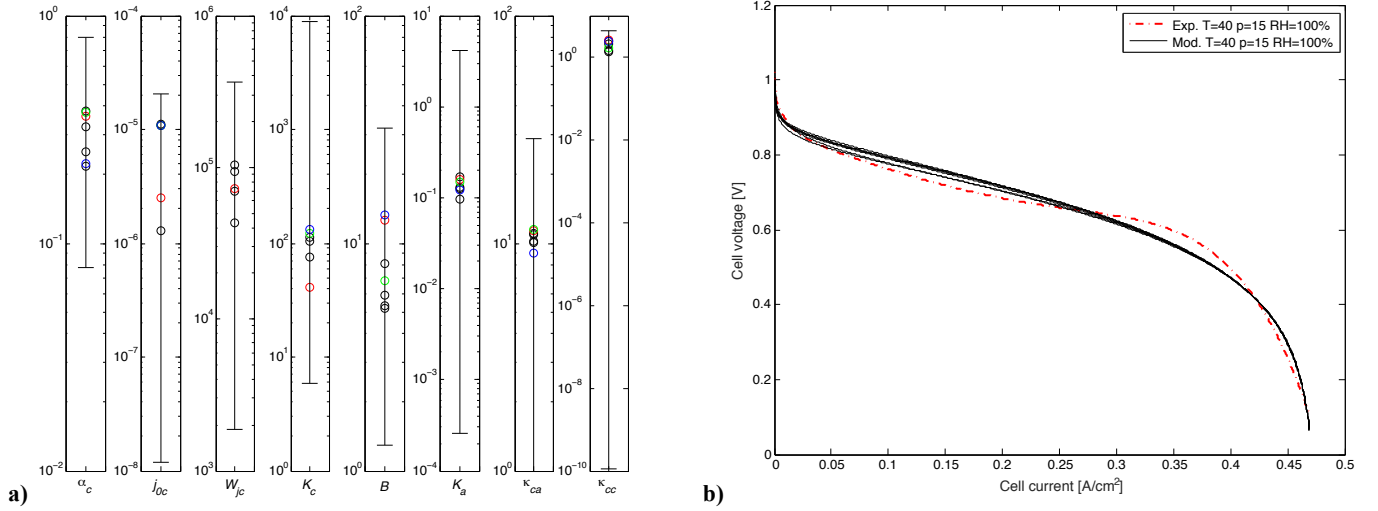


Fig. 8. Stochastic effect - Seven best optimizations after 20 runs a) Distribution of the best optimized parameters; b) resulting modeled polarization curves

Table 4: Model parameters identified by means of the hybrid PSO-DE algorithm.

	α_c	j_{0c} μAcm^{-2}	W_{jc} J mol^{-1}	J_{cod} mAcm^{-2}	K_c cm s^{-1}	K_a cm s^{-1}	κ_{ca}	κ_{cc}	B	ζ $\times 10^{-3}$	k_{t1} $\text{K cm}^2\text{A}^{-1}$	k_{t2} $\text{K cm}^4\text{A}^{-2}$
T = 40°C p _i = 15 psig RH = 100%	0.33	1.71	43218	0.23	97.3	0.314	11.2	2.21	7.79	8.4	2.04	8.09
T = 60°C p _i = 15 psig RH = 100%	0.39	1.71	41883	0.32	120.5	0.352	12.1	1.97	6.70	9.2	1.95	8.13
T = 85°C p _i = 15 psig RH = 100%	0.37	1.71	47430	0.097	98.4	0.499	10.8	2.01	8.57	8.5	2.21	7.77
T = 40°C p _i = 65 psig RH = 100%	0.37	1.68	47451	0.24	100.2	0.134	11.2	1.88	2.81	8.7	1.98	7.69
T = 60°C p _i = 65 psig RH = 100%	0.43	1.66	48618	0.099	97.4	0.136	11.4	1.96	5.79	9.1	2.20	8.01
T = 85°C p _i = 65 psig RH = 100%	0.61	1.68	46414	0.24	131.3	0.185	12.2	2.04	5.10	9.7	1.79	8.11
T = 40°C p _i = 15 psig RH = 50%	0.52	1.84	43538	0.29	120.0	0.346	10.8	1.98	2.88	31	2.31	8.14

T = 60°C p _i = 15 psig RH = 50%	0.51	1.86	54173	0.17	99.8	0.398	11.4	2.09	19.3	29	1.96	7.88
T = 85°C p _i = 15 psig RH=50%	0.53	1.85	32965	0.20	101.1	0.498	12.0	2.11	13.3	31	1.97	8.34
T = 40°C p _i = 65 psig RH = 50%	0.35	1.17	44391	0.099	122.3	0.117	11.3	1.89	12.9	32	2.02	7.90
T = 60°C p _i = 65 psig RH = 50%	0.37	1.16	45432	0.17	109.6	0.146	11.9	1.92	23.3	29	2.02	7.95
T = 85°C p _i = 65 psig RH = 50%	0.40	1.17	42519	0.19	102.3	0.196	11.9	1.98	51.3	32	1.91	8.18

6.4. Lessons learned

Some final considerations emerge after performing the parameters identification and the consequent model fitting to the experimental curves. First, the larger the number of unknown parameters, the wider and more accurate must be the experimental data and the experimental conditions. Such accuracy may be critical to obtain in the case of experimental data consisting of the polarization curves of a fuel cell, which depend on a large number of factors related to both the samples under test and the experimental conditions, some of which are hard to repeat with high accuracy. Such difficulties can be dealt with by collecting more curves in the same operating conditions, which allows us to perform a quality control of the materials used in preparing the samples and make a statistical selection of the experimental data. Moreover, enriched experimental conditions may allow to identify also some parameters which have a minor effect on the polarization curve, e.g. a set of experimental data captured with different back pressures between anode and cathode may allow the identification of the anodic exchange current density, which is otherwise hidden by the larger effect of the cathodic exchange current density. This issue confirms that accurate parameter identification in fuel cells is a “no-free-lunch” task [13]. On the other hand, the identification procedure, or, more precisely, the poorly accurate fitting of the whole polarization curves over every operating condition, can be instrumental in revealing weakness factors of the model, calling for further work for its improvement and enrichment, so as to take into account hidden and subtle effects.

7. Conclusions

As reported in previous literature, stochastic optimizers have already proven to be particularly effective for fitting models depending on a large number of parameters to experimental data, as is the case of PEMFC numerical models which aim at reproducing their polarization curve. The challenge we have faced consists in using stochastic optimizers for the identification of multiple physical parameters via *in situ* measurements. Our work highlights that this is a much more challenging task than simply fitting empirical models, but it is feasible. To achieve this aim, care and work are required, as regards model accuracy and optimization strategy. The results can be of great importance in addressing future research on materials. Comparison of the results with *ex situ* measurements also allows us to address the pathways for transferring the performance parameters to fuel cell operative conditions. Better performance can be achieved using optimization algorithms tailored to the problem at hand and the operator’s expertise is crucial to fit the algorithm formulation to the required parameters. Wider ranges of experimental data, such as curves extended to extreme current density values and resolved at different operating conditions ($T, p, p_a \neq p_c, RH, RH_a \neq RH_c$), assure a wider knowledge of the problem that can fully exploit the stochastic optimizer capabilities. Duplicity problems are lurking in this kind of identification, but they can be prevented by means of stepwise and selective procedures incorporating the stochastic optimizer as a core processor, which result in variable separation techniques. Finally, stochastic optimization can reveal physical model weaknesses and can suggest model improvements.

Acknowledgements

This work was supported by the University of Padua within its 2011 strategic project MAESTRA, which aims at developing the technology of advanced storage devices for both stationary and mobile applications.

References

- [1] Li Q, Jensen JO, Savinell RF, Bjerrum NJ. High temperature proton exchange membranes based on polybenzimidazoles for fuel cells. *Progress in Polymer Science (Oxford)* 2009; 34; 5: 449-477.
- [2] Alotto P, Guarnieri M, Moro F, Stella A. Multi-physic 3D dynamic modelling of polymer membranes with a proper generalized decomposition model reduction approach. *Electrochimica Acta* 2011; 57: 250-256.
- [3] Di Noto V, Guarnieri M, Moro F. A Dynamic Circuit Model of a Small Direct Methanol Fuel Cell for Portable Electronic Devices. *IEEE Transactions on Industrial Electronics* 2010; 57; 6: 1865-1873.
- [4] Stevens DA, Hicks MT, Haugen GM, Dahn JR. Ex situ and in situ stability studies of PEMFC catalysts effect of carbon type and humidification on degradation of the carbon. *Journal of the Electrochemical Society* 2005; 152; 12: A2309-A2315.
- [5] Yuan X, Wang H, Colin Sun J, Zhang J, AC impedance technique in PEM fuel cell diagnosis-A review. *International Journal of Hydrogen Energy* 2007; 32; 17: 4365-4380.
- [6] Jaouen F, Herranz J, Lefèvre M, Dodelet J-P, Kramm UI, Herrmann I, Bogdanoff P, Maruyama J, Nagaoka T, Garsuch A, Dahn JR, Olson T, Pylypenko S, Atanassov P, Ustinov EA. Cross-laboratory experimental study of non-noble-metal electrocatalysts for the oxygen reduction reaction. *ACS Applied Materials and Interfaces* 2009; 1; 8: 1623-1639.
- [7] Owejan JP, Gagliardo JJ, Sergi JM, Kandlikar SG, Trabold TA. Water management studies in PEM fuel cells, Part I: Fuel cell design and in situ water distributions. *International Journal of Hydrogen Energy* 2009; 34; 8: 3436-3444.
- [8] Bazylak A, Sinton D, Liu Z-S, Djilali N. Effect of compression on liquid water transport and microstructure of PEMFC gas diffusion layers. *Journal of Power Sources* 2007; 163; 2: 784-79.
- [9] Hickner MA, Siegel NP, Chen KS, Hussey DS, Jacobson DL, Arif M, In situ high-resolution neutron radiography of cross-sectional liquid water profiles in proton exchange membrane fuel cells. *Journal of the Electrochemical Society* 2008; 155; 4: B427-B434.
- [10] Bellman RE. *Dynamic programming*. Princeton University Press 1957.
- [11] Schrijver A. *Theory of Linear and Integer Programming*. John Wiley & Sons 1998.
- [12] Bazaraa MS, Sherali HD, Shetty CM. *Nonlinear Programming: Theory and Algorithms*. Hoboken NJ: John Wiley & Sons 2005.
- [13] Wolpert DH, Macready WG. No Free-Lunch Theorems for Optimization. *IEEE Transactions on Evolutionary Computation* 1997; 1; 1: 67-82.
- [14] Alotto P, Guarnieri M. Stochastic Methods for Parameter Estimation of Multiphysics Models of Fuel Cells. *IEEE Transactions on Magnetics* 2014; 50; 2: # 7017304.
- [15] Guarnieri M, Alotto P, Moro F. Modeling the Performance of H₂-O₂ Unitized Regenerative PEM Fuel Cells for Energy Storage. *Journal of Power Sources* 2015; 297; 11; 23-32.
- [16] Bard AJ, Faulkner LR. *Electrochemical Methods, Fundamentals and Applications*. New York: John Wiley & Sons; 2006.
- [17] NIST Chemistry WebBook - Standard Reference Database Number 69. <http://webbook.nist.gov/chemistry/>
- [18] O'Hayre R, Cha SW, Coltella W, Prinz FB. *Fuel Cell Fundamentals*. New York: John Wiley & Sons, 2009, pp. 195-202.
- [19] Di Noto V, Negro E. Development of nano-electrocatalysts based on carbon nitride supports for the ORR Processes in PEM Fuel Cells. *Electrochimica Acta* 2010; 55: 7564-7574.
- [20] Parthasarathy A, Srinivasan S, Appleby AJ, Martin CR. Temperature dependence of the electrode kinetics of oxygen reduction at the platinum/Nafion® interface – a microelectrode investigation. *Journal of the Electrochemical Society* 1992; 139; 9: 2530-2537.
- [21] You L, Liu H. A two-phase flow and transport model for the cathode of PEM fuel cells. *International Journal of Heat Mass Transfer* 2002; 45; 11: 2277-2287.
- [22] Kays WM, Crawford ME. *Convective Heat and Mass Transfer*, McGraw-Hill, New York, 1993.
- [23] Mench MM, *Fuel Cell Engines*, Wiley, Hoboken, 2008.
- [24] Di Noto V, Zawodzinski TA, Herring AM, Giffin GA, Negro E, Lavina S. Polymer electrolytes for a hydrogen economy. *International Journal of Hydrogen Energy* 2012; 37; 7: 6120-6131.
- [25] Springer TE, Zawodzinski TA, Gottesfeld S. Polymer electrolyte fuel cell models. *Journal of the Electrochemical Society* 1991; 138; 8: 2334-2341.
- [26] Di Noto V, Piga M, Pace G, Negro E, Lavina S. Dielectric relaxations and conductivity mechanism of Nafion: Studies based on broadband dielectric spectroscopy. *ECS Transactions* 2008; 16; 2: 1183-1193.
- [27] Sequeira C, Santos D. *Polymer electrolytes – Fundamentals and Applications*. Woodhead Publ 2010: 219-277.
- [28] Di Noto V, Lavina S, Wintersgill MC, Fontanella JJ. A formalism relating the conductivity of functionalized nanoparticles to constituent ligand molecules and application to water-containing silica, *Physical Chemistry Chemical Physics* 2010; 12: 5993-5997.
- [29] Tsushima S, Hirai S. In situ diagnostics for water transport in proton exchange membrane fuel cells. *Progress in Energy and Combustion Science* 2011; 37: 204-220.
- [30] Baik KD, Kong IM, Hong BK, Kim SH, Kim MS. Local measurements of hydrogen crossover rate in polymer electrolyte membrane fuel cells. *Applied Energy* 2013; 101: 560-566.
- [31] Vilekar SA, Datta R. The effect of hydrogen crossover on open-circuit voltage in polymer electrolyte membrane fuel cells. *Journal of Power Sources* 2010; 195; 8: 2241-2247.
- [32] Carnes B, Djilali N. Systematic parameter estimation for PEM fuel cell models. *Journal of Power Sources* 2005; 144: 83-93.
- [33] Chevalier S, Trichet D, Auvity B, Olivier JC, Josset C, Machmoum M. Multiphysics DC and AC models of a PEMFC for the detection of degraded cell parameters. *International Journal of Hydrogen Energy* 2013; 38; 26: 11609-11618.
- [34] Ettihir K, Boulon L, Becherif M, Agbossou K, Ramadan HS. Online identification of semi-empirical model parameters for PEMFCs. *International Journal of Hydrogen Energy* 2014; 39; 36: 21165-21176.
- [35] Zhong ZD, Zhua XJ, Cao GY. Modeling a PEMFC by a support vector machine. *Journal of Power Sources* 2006; 160: 293-298.
- [36] Li X, Cao GY, Zhu XJ. Modeling and control of PEMFC based on least squares support vector machines. *Energy Conversion and Management* 2006; 47: 1032-1050.

- [37] Li Z, Giurgea, S Outbib, R, Hissel, D. Online Diagnosis of PEMFC by Combining Support Vector Machine and Fluidic Model. *Fuel Cells* 2014; 14; 3: 448-456.
- [38] Secanell M, Carnes B, Suleman A, Djilali N. Numerical optimization of proton exchange membrane fuel cell cathodes. *Electrochimical Acta* 2007; 52: 2668-82.
- [39] Cheng CH, Lin HH, Lai GH. Design for geometric parameters of PEM fuel cell by integrating computational fluid dynamics code with optimization method. *Journal of Power Sources* 2007; 165; 2: 803-813.
- [40] Wang XD, Huang YX, Cheng CH, Jang JY, Lee DJ, Yan WM, Su A. Flow field optimization for proton Exchange membrane fuel cells with varying channel heights and widths. *Electrochimical Acta* 2009; 54: 5522-5530.
- [41] Berg P, Kimmerle SJ, Novruzi A. Modeling, shape analysis and computation of the equilibrium pore shape near a PEM-PEM intersection. *Journal of Mathematical Analysis and Applications* 2014; 410; 1: 241-256.
- [42] Petrone R, Zheng Z, Hissel D, Péra MC, Pianese C, Sorrentino M, Becherif M, Yousfi-Steiner N. A review on model-based diagnosis methodologies for PEMFCs, *International Journal of Hydrogen Energy* 2013; 38: 7077-7091.
- [43] Ohenoja M, Leiviska, K. Validation of genetic algorithm results in fuel cell model. *International Journal of Energy Research* 2010; 35; 22: 12618-12625.
- [44] Zhang L, Wang N. An adaptive RNA genetic algorithm for modeling of proton exchange membrane fuel cells. *International Journal Hydrogen Energy* 2013; 38; 1: 219-228.
- [45] Li Q, Chen W, Wang Y, Liu S. Parameter Identification for PEM Fuel-Cell Mechanism Model Based on Effective Informed Adaptive Particle Swarm Optimization. *IEEE Transaction on Industrial Electronics* 2011; 58; 6: 2410-2419.
- [46] Chang WY. Equivalent circuit parameters estimation for PEM fuel cell using RBF neural network and enhanced Particle Swarm Optimization. *Mathematical Problems in Engineering* 2013 (2013), # 672681.
- [47] Huang S-R, Wu C-C, Lin C-Y, Chen H-T. Parameter optimization of the biohydrogen real time power generation system using differential evolution algorithm. *International Journal of Hydrogen Energy* 2010; 35; 13: 6629-6633.
- [48] Chakraborty UK, Abbott TE, Das SK. PEM fuel cell modeling using differential evolution. *Energy* 2012; 40; 1: 387-399.
- [49] Booker LB, Goldberg DE, Holland JH. Classifier systems and genetic algorithms. *Artificial Intelligence* 1989; 40; 1-3: 235-282.
- [50] Kennedy J, Eberhart R. Particle Swarm Optimization. *Proceedings of IEEE International Conference on Neural Networks IV* 1995: 1942-1948.
- [51] Storn R, Price K. Differential Evolution - A Simple and Efficient Adaptive Scheme for Global Optimization over Continuous Spaces. Tech. Report, International Computer Science Institute (Berkeley) Technical Report 1995.
- [52] Storn R, Price K. Differential Evolution – A Simple and Efficient Heuristic for global Optimization over Continuous Spaces. *Journal of Global Optimization* 1997; 11: 341-359.
- [53] Ishibashi KI, Kimura Y, Niwano M, An extensively valid and stable method for derivation of all parameters of a solar cell from a single current-voltage characteristic. *Journal of Applied Physics* 2008; 103: # 094507.
- [54] Úbeda D, Pinar FJ, Cañizares P, Rodrigo MA, Lobato J. An easy parameter estimation procedure for modeling a HT-PEMFC, *International Journal of Hydrogen Energy* 2012; 37: 11308-11320.
- [55] Chang WY. Application of current switching method to estimate the model parameters of proton exchange membrane fuel cell. *Simulation Modelling* 2010; 18: 35-50.
- [56] Chang WY. Estimating equivalent circuit parameters of proton exchange membrane fuel cell using the current change method. *Electrical Power and Energy Systems* 2013; 53: 584-591.
- [57] Di Noto V, Negro E, Polizzi S, Vezzù K, Toniolo L, Cavinato G. Synthesis, studies and fuel cell performance of “core-shell” electrocatalysts for oxygen reduction reaction based on a PtNix carbon nitride “shell” and a pyrolyzed polyketone nanoball “core”. *International Journal of Hydrogen Energy* 2014, 39: 2812-2827.
- [58] Di Noto V, Piga M, Piga L, Polizzi S, Negro E, New inorganic-organic proton conducting membranes based on Nafion® and [(ZrO2)·(SiO2)0.67] nanoparticles: Synthesis vibrational studies and conductivity. *Journal Power Sources* 2008; 178: 561-574.

Nomenclature

Acronyms

BES	broadband electrical spectroscopy
BP	bipolar plate
CV-TF-RRDE	cyclic voltammetry with the thin-film rotating ring-disc electrode
DE	differential evolution
DL	diffusion layer
DMFC	direct methanol fuel cells
EIS	electrochemical impedance spectroscopy
FC	fuel cell
MCFC	molten carbonate fuel cells
PEMFC	proton exchange membrane fuel cells
PSO	particle swarm optimization
SOFC	solid oxide fuel cells
VTF	Vogel-Tamman-Fulcher

Symbols in stochastic optimization

A	search space
c_1, c_2	learning factors
CR	crossover ratio
f	objective, quality, fitness, or cost function
F_1, F_2	mutation factors
f_1, f_2	partial fitness functions
I	random integer
I	random integer
n	dimension of \mathbf{R}^n , number of variables to be optimized, number of particles
p	personal best
\mathbf{R}	set of the real numbers
\mathbf{R}^n	n-dimensional set of the real numbers
r_1, r_2	randomly generated numbers
R_{ij}	uniformly distributed random real number
t	number of iterations
u	trial
v	velocity
w	weight
x	element of the search space, candidate solution
w_1, w_2	partial objective weights
x^*	maximum, minimum of the search space, solution of the optimization problem

y	donor
-----	-------

Symbols in fuel cell model

A	cell active cross-section	cm^2
A_{TPB}	total triple phase boundaries area	cm^2
A_0	VTF conductivity parameter	$\text{K}^{0.5} \text{S cm}^{-1}$
a_w	water activity	
B	dimensionless conductivity coeff.	
b	concentration voltage drop coeff.	V
c	concentration	mol cm^{-3}
D	diffusivity	$\text{cm}^2 \text{s}^{-1}$
d	thickness	cm
E	Nernst cell voltage	V
E^0	Standard Nernst cell voltage	V
F	Faraday constant	C mol^{-1}
f_e	electrochemical parameter	K V^{-1}
g	dimensionless gas fraction	
i	electric current	A
j	electric current density	A cm^{-2}
\mathbf{j}, \mathbf{N}	vectors of j, N	
j_0	exchange current density	A cm^{-2}
j_{co}	equivalent crossover current density	A cm^{-2}
j_{cod}	equivalent diffusive crossover current density	A cm^{-2}
j_{coe}	equivalent electro-osmotic crossover current density	A cm^{-2}
j_L	limit crossover current density	A cm^{-2}
j_t	total current density	A cm^{-2}
K	mass transfer coefficient	cm s^{-1}
k_t	global thermal exchange coefficient	K W^{-1}
k_{t1}	1 st thermal exchange coefficient	$\text{K cm}^2 \text{A}^{-1}$
k_{t2}	2 nd thermal exchange coefficient	$\text{K cm}^4 \text{A}^{-2}$
n	charge carriers per reaction	
N	gas molar flow	$\text{mol cm}^{-2} \text{s}^{-1}$
p	pressure	Pa
P_a	kinetic activity dissipation per unit area	W cm^{-2}
P_{diss}	total dissipation per unit area	W cm^{-2}
p_l	total bulk pressures	kPa
P_m	membrane dissipation per unit area	W cm^{-2}
P_p	thermodynamic dissipation per unit area	W cm^{-2}
p_w	vapor pressure	kPa
p_{ws}	vapor saturation pressure	kPa

R	gas constant	$\text{J mol}^{-1} \text{K}^{-1}$
R_{col}	collector ohmic resistance	Ω
RH	relative humidity	%
R_m	membrane ohmic resistance	Ω
R_{ohm}	ohmic resistance	Ω
Sh	Sherwood number	
T	temperature	K
T_g	glass transition temperature	K
T_r	room temperature	K
W	activation barrier	J mol^{-1}
α	transfer coefficient	
γ	membrane conductivity	S cm^{-1}
γ_0	membrane conductivity at $\lambda = 0.115$	S cm^{-1}
Δ	variation, increment	
ΔE_c	Nernst voltage variation with c	V
ΔE_s	Nernst voltage variation with $\Delta \hat{s}$	V
ΔV_a	activation voltage drop	V
ΔV_c	concentration voltage drop	V
ΔV_m	membrane ohmic voltage drop	V
ΔV_{ohm}	ohmic voltage drop	V
ε	DL porosity	
ζ	electro-osmotic drag coefficient	
κ	coefficient in concentration losses	
λ	membrane hydration	
ρ_e	surface electric charge density	C cm^{-2}
τ	Bruggeman coefficient	
B	membrane conductivity coefficient	
$\Delta \hat{s}$	molar reaction entropy	$\text{J mol}^{-1} \text{K}^{-1}$
$\Delta \hat{h}$	molar reaction enthalpy	J mol^{-1}
$\Delta \hat{g}$	molar reaction Gibbs free energy	J mol^{-1}
∂_t	partial time derivative	
∇	nabla operator	

Subscripts and superscripts in fuel cell model

<i>aa</i>	activation anodic
–	(upper) bulk value
*	reference value
<i>a</i>	anode
<i>A</i>	cross-section area
<i>ac</i>	activation cathodic
<i>A_{TPB}</i>	electrochemical active area (i.e. at TPB)
<i>c</i>	cathode
<i>ca</i>	concentration anodic
<i>cc</i>	concentration cathodic
<i>cl</i>	concentration in load condition
<i>co</i>	concentration in open circuit
<i>col</i>	collector
<i>dl</i>	diffusion layer
<i>e</i>	electrical
<i>eff</i>	effective
<i>fc</i>	flow channel
H ₂	hydrogen
<i>m</i>	membrane
<i>mH₂</i>	hydrogen in the membrane
O ₂	oxygen
<i>OC</i>	open circuit
<i>ohm</i>	ohmic
<i>P</i>	product
<i>R</i>	reagent
<i>sa</i>	sulfonic acid groups
<i>TPB</i>	triple phase boundaries
<i>x</i>	species/electrode index